J Mater Sci (2011) 46:6054–6064
DOI 10.1007/s10853-011-5567-8

# Mesoscopic nonequilibrium thermodynamics treatment of the grain boundary thermal grooving induced by the anisotropic surface drift diffusion

**Oncu Akyildiz · Ersin Emre Oren ·**
**Tarik Omer Ogurtani**

Received: 31 December 2010 / Accepted: 16 April 2011 / Published online: 3 May 2011

**Abstract** A systematic study based on the self-consistent dynamical simulations is presented for the grain boundary thermal grooving problem by strictly following the irreversible thermodynamic theory of surfaces and interfaces with singularities [T. O. Ogurtani, J. Chem. Phys. 124, 144706 (2006)]. This approach furnishes us to have autocontrol on the otherwise free-motion of the grain boundary triple junction without presuming any equilibrium dihedral (wetting) angles at the edges. The effects of physicochemical properties and the anisotropic surface diffusivity on the transient grooving behavior, which takes place at the early stage of the scenario, were considered. We analyzed the experimental thermal grooving data reported for tungsten in the literature, and compared them with the carried simulation results. This investigation showed that the observed changes in the dihedral angles are strictly connected to the transient behavior of the simulated global system, and manifest themselves at the early stage of the thermal grooving phenomenon.

## Abbreviations

| | |
|---|---|
| GB | Grain boundary |
| TJ | Triple junction |
| AFM | Atomic force microscopy |
| WP | Wetting parameter |
| BC | Boundary conditions |

O. Akyildiz · T. O. Ogurtani (✉)
Department of Metallurgical and Materials Engineering, Middle East Technical University, 06531 Ankara, Turkey
e-mail: ogurtani@metu.edu.tr

E. E. Oren
Department of Biomedical Engineering, TOBB University of Economics and Technology, 06560 Ankara, Turkey
e-mail: eeoren@etu.edu.tr

## Introduction

Thermal grooving at the grain boundaries is a process of capillary-driven evolution of surface topography in the region where a grain boundary (GB) emerges to intersect a free surface of a polycrystalline material. Surface diffusion is reported as the dominant mass transport mechanism in several cases [1]. The earliest study of the grooving of a GB was Mullins' [2] treatment, which relies strictly on the equilibrium thermodynamics including Gibbs' description of interfaces and surfaces [3, 4]. Mullins ignored GB diffusion and considered the triple junction (TJ) to have the equilibrium capillarity configuration satisfying the Young [5] relationship. The boundary conditions set by Mullins have been used by several researchers to investigate not only the thermal grooving [6–9], but also some related phenomena like propagation of GB slits during electromigration [10–14], GB cavity growth under tensile stresses [15–18] without questioning the nonequilibrium nature of the TJ motion.

The present article utilizes a mathematical model based on the nonequilibrium thermodynamics treatment of the TJ singularity by Ogurtani [19–21]. This model was first applied by Oren and Ogurtani [22] to investigate the problem of intergranular void motion, and later by Ogurtani and Akyildiz [23–25] for GB grooving and cathode voiding in finite thin film interconnects with bamboo structures under the action of capillary and electromigration forces. The latter works show the existence of a transient regime that is completely overlooked by researchers employing methods based on reversible processes and the true equilibrium states. As an application of the proposed mesoscopic nonequilibrium theory, we will present an analysis of the data provided from the 3D atomic force microscopy (AFM) images [26] at each annealing time of tungsten held in vacuum at 1,350 °C, and investigate the effects of material specific physicochemical parameters on the thermal grooving.

## Physical and mathematical modeling

The present irreversible thermodynamic model, which was developed for the ordinary points as well as for the TJ singularities by Ogurtani [19–21] considers not only the drift–diffusion of chemical species along the realistic surfaces and interfaces, but also the direct transfer of chemical species (condensation and evaporation) between bulk phase and the adjacent vapor (realistic void) or condensed phases such as secondary phase particles.

The evolution kinematics of surfaces or interfacial layers (simply connected domains) may be described by the following well-posed moving boundary value problem in 2D space, respectively, for the ordinary points and the TJ singularities, in terms of normalized and scaled parameters and variables. In these formulas, the surface drift–diffusion, which may be represented by an angular dependent post factor, $D(\theta, \phi)$, has been taken as anisotropic. On the other hand, the specific Gibbs free energies, associated with the groove surfaces and the grain boundary interfacial layer, have been assumed to be isotropic to simplify the problem. The surface displacement velocity denoted by $\bar{V}_{\text{ord}}$ at the ordinary points is given by the following governing equation in the normalized and scaled space:

$$\bar{V}_{\text{ord}} = \frac{\partial}{\partial \bar{\ell}}\left[D(\theta, \phi)\frac{\partial}{\partial \bar{\ell}}(\Delta \bar{g}_{vb} + \bar{\kappa})\right] - \bar{M}_{vb}(\Delta \bar{g}_{vb} + \bar{\kappa}) \tag{1}$$

where $\bar{\kappa}$ is the local curvature and is taken to be positive for a convex void or a concave solid surface (trough), $\bar{\ell}$ is the curvilinear coordinate along the void surface (arc length). $\Delta \bar{g}_{vb} = (\bar{g}_v - \bar{g}_b)$ denotes the normalized volumetric Gibbs free energy density difference between the realistic void phase (vapor) and the bulk matrix ($\Delta \bar{g}_{vb} < 0$ evaporation or void growth), and it is normalized with respect to the specific surface Gibbs free energy of the groove surface layer denoted by $g_\sigma$. In Eq. 1, the bar signs over the letters indicate the following scaled and normalized quantities:

$$\bar{t} = t/\tau_{\text{o}}, \quad \bar{\ell} = \ell/\ell_{\text{o}}, \quad \bar{\kappa} = \kappa \ell_{\text{o}}, \quad \bar{W} = W/\ell_{\text{o}}, \quad \bar{L} = L/\ell_{\text{o}} \tag{2}$$

$$\Delta \bar{g}_{vb} = \frac{g_{vb}\ell_{\text{o}}}{g_\sigma}, \; \bar{M}_{vb} = \frac{\hat{M}_{vb}\ell_{\text{o}}^2}{\hat{M}_\sigma} \tag{3}$$

The time and space variables $\{t, \ell\}$ have been scaled in the following fashion: at first we defined the atomic surface mobility $\hat{M}_\sigma$ associated with mass flow at the surface layer by the relationship $\hat{M}_\sigma = [D_\sigma h_\sigma / kT\Omega_\sigma]$, where $D_\sigma$ is the surface diffusion coefficient, $h_\sigma$ is the thickness of the surface layer, $\Omega_\sigma$ is the mean atomic volume of chemical species at the surface layer, and $kT$ has the usual meaning. Then a new time scale is introduced by $\tau_{\text{o}} = \ell_{\text{o}}^4 / \left(\Omega_\sigma^2 \hat{M}_\sigma g_\sigma\right)$, where $\ell_{\text{o}}$ is the arbitrary length scale, which is for the present simulation studies chosen as $\ell_{\text{o}} = W$, where $W$ and $L$ are the half width and length of the bicrystal specimen, respectively. $\hat{M}_{vb}$ is the generalized mobility associated with the interface displacement reaction (i.e., phase transformation) taking place during the growth process by evaporation or condensation phenomenon.

Triple junction drift velocity along a rigidly fixed GB layer can be represented by:

$$\bar{V}_g^{\text{long}} = \bar{M}^{\text{long}} \frac{\bar{\Omega}_g \bar{d}_a}{2\bar{\Omega}_\sigma^2 \bar{h}_g}\left[2\lambda - \left(\cos\theta^+ + \cos\theta^-\right)\right] \tag{4}$$

where $\bar{d}_a$, and $\bar{h}_g$ are the interatomic distance and the thickness of the GB layer, respectively. $\bar{\Omega}_g$ and $\bar{\Omega}_\sigma$ are mean atomic volumes of chemical species, respectively, in the GB and the void surface layer. $\bar{M}^{\text{long}} = \hat{M}^{\text{long}} / \hat{M}_\sigma$ is the normalized longitudinal mobility of the TJ, which is defined by $\hat{M}^{\text{long}} = \frac{\Re^{\text{long}}}{kT} \frac{h_g}{\Omega_g}$. Where, $\Re^{\text{long}}$ is the transition rate associated with the mass exchange between the grain boundary region and the adjacent surface layers during the longitudinal displacements of the TJ, which may be calculated by Eyring [27] transition rate theory. $\lambda$ is the *wetting parameter* associated with the TJ, and assumed to be isotropic. It may be given by $\lambda = g_g / 2g_\sigma$, where $g_g$ and $g_\sigma$ are the specific surface Gibbs free energy densities, respectively, for the grain boundary and groove surface layers.

The following boundary conditions (BC) at the TJ in terms of right and left side fluxes may be written as:

$$\begin{aligned} \bar{J}_{\text{o}}^{\mp} = {} & \mp \bar{M}^{\text{long}} \frac{\bar{d}_a}{2\bar{\Omega}_\sigma^2}(\lambda - \cos\theta^{\mp}) \mp \bar{J}_g/2 + \bar{J}_\vartheta \\ & + \bar{M}^{\text{trans}} \frac{\bar{d}_a}{\bar{\Omega}_\sigma^2}\left(\sin\theta^+ - \sin\theta^-\right) \end{aligned} \tag{5}$$

In Eq. 5, the ($\mp$) first group of terms represents the material lost from the TJ-edge of the GB layer due to shortening of its length caused by the GB–TJ longitudinal motion, and then injected equally into the both branches of the surface layer to extend its length (in situ 2D-phase transition). The last group of terms corresponds to the material transfer from one side of the surface layer to another side through the GB–TJ to compensate the possible asymmetry in the surface profile, and then try to approach a nonequilibrium stationary state profile having symmetrically disposed configuration in the absence of the so-called Herring's torque term [19]. Here, the particular partition of the incoming GB flux $\bar{J}_g$ between $\bar{J}_o^+$ and $\bar{J}_{\text{o}}^-$ at the GB–TJ is a matter of convenience; otherwise it is completely arbitrary as long as one satisfies the generalized law of conservation of particles including the in situ phase transformation at the TJ. $\bar{J}_g$ denotes the normalized atomic fluxes associated with the GB mass flow due to some driving force such as thermal stress field inhomogeneities. Similarly, $\bar{J}_\vartheta$ is the contribution due to external forces (e.g., electromigration) acting on the both branches of the groove at the TJ.

In Eq. 5, the following scaled and normalized quantities were employed: $\bar{M}^{\text{trans}}$ corresponds to the normalized transverse mobility of the TJ with respect to $\hat{M}_\sigma$. The explicit expressions may be given by:

$$\hat{M}^{\text{trans}} = \frac{\mathfrak{R}^{\text{trans}}}{kT}\frac{h_\sigma}{\Omega_\sigma}, \hat{M}_{gb} = \frac{D_g}{kT}\frac{h_g}{\Omega_g} \quad (6)$$

where, similarly $\mathfrak{R}^{\text{trans}}$ is the transition rate associated with the atomic flow of chemical species across the TJ from one side of the groove surface to another side in order to establish lateral or transverse force balance at the stationary state, which may be calculated by Eyring [27] transition rate theory. $D_g$ and $D_\sigma$ are the GB and surface diffusion coefficients, respectively. In the formulation of the problem, we adapted a convention such that the positive direction of the motion is always toward the bulk material whether one deals with inner voids or outer surfaces or interfaces.

A careful examination of Eqs. 4 and 5 shows immediately that there is no conservation of fluxes at the TJ in ordinary sense. This is due to the phase transformation taking place during the displacement of the TJ (positive internal entropy production), which is precisely accounted by Eq. 4. If one combines incoming $\bar{J}_\sigma^-$ and outgoing $\bar{J}_\sigma^+$ conjugated fluxes at the TJ by using Eq. 5, and recalls that the clockwise direction is chosen as the positive direction for fluxes, then the following universal connection in the presence of Eq. 4 is obtained, namely the conservation of chemical species including the phase transformation at TJ:

$$\bar{J}_\sigma^- + \bar{J}_g - \bar{J}_\sigma^+ + \bar{V}_g^{\text{long}}\bar{h}_g\bar{\Omega}_g^{-1} \equiv 0 \quad (7)$$

where, the final term on the left hand side represents the rate of material discharge or gain by the GB during the displacement of the TJ along the GB. Similarly, $\bar{J}_g$, is the incoming material flux from the GB to TJ.

For a disconnected interfacial layer (finite or infinite) such as one or two-grain sector of interconnect, additional BCs should be set at the end points of the metallic line. We employed reflecting BC that does not allow any material flow or leakage through the specimen ends due to the drift–diffusion caused by the chemical and capillary forces. The net flux at the edge may be written in the normalized and scaled time and space domain as:

$$\bar{J}_\sigma^{\text{edge}} = \frac{D''(\theta,\phi)}{\bar{\Omega}_\sigma}\frac{\partial}{\partial\ell}[\Delta\bar{g}_{vb} + \bar{\kappa}] \equiv 0 \quad (8)$$

The system of equations given above, Eqs. 1–8, describe highly nonlinear and well-posed free and moving boundary problem in two dimensional space, which can be easily handled in discretized space. The procedure used in the numerical treatment of the problem is fully discussed in our previous papers [19–25] and will not be repeated here.

## Results and discussions

### Thermal grooving revisited: the effect of physicochemical parameters

In this section, we will present our extensive computer simulation studies, performed on the thermal grooving induced by the isotropic surface drift diffusion and driven by the capillary forces. The simulation results are analyzed for a given set of initial data. Here, the initial configurations of the reported systems are always a flat surface having a freshly formed GB cutting the crystal into two pieces. Accordingly, the groove tip displacement is measured with respect to the original surface and the positive direction is chosen toward the bulk. The simulations are performed by using a large range of wetting parameters (WP) $\lambda \subset [0.16 - 0.95]$ and the GB TJ mobilities $\bar{M}^{\text{long}}, \bar{M}^{\text{trans}} \subset [0.001 - 1]$. Only the few relevant results will be presented here explicitly to economize the space.

Figure 1a, b demonstrates the morphological evolution behavior of a thermal groove as a function of the normalized time utilizing 3D and 2D computer graphics, respectively. These simulations may be characterized by a set of TJ mobilities such as $\bar{M}^{\text{long}} = \bar{M}^{\text{trans}} \subset (1 - 0.25)$, and a WP given by $\lambda = 0.5$. Here, we intentionally selected relatively high normalized TJ mobilities in order to stay close to the Mullins' regime [21]. The curvature plot given in the lower portion of the Fig. 1b has an undefined point (i.e., singularity) at the groove root ($X = 0$). Since the longitudinal and transverse motions of the TJ are defined at that point by the boundary conditions, which do not involve curvature at the TJ, as deduced from the irreversible thermodynamic theory of surfaces and interfaces, this singularity does not constitute any problem in the computations.

Analysis of the normalized penetration depth versus time data given in Fig. 1c shows that the system reaches a stationary state regime roughly around $t = 0.01$, and stays there till the end of the experiment with a time exponent of 0.25. This regime defines a time independent groove shape having linear dimensions changing with $t^{1/4}$, which agrees with the analytic solution for surface diffusion dominant mass transport introduced originally by Mullins [2]. Ogurtani and Akyildiz [23], and Ramasubramaniam and Shenoy [28], in their simulation studies for the symmetrically disposed GB grooving, have independently recovered Mullins' isotropic one-fourth power law for their large TJ

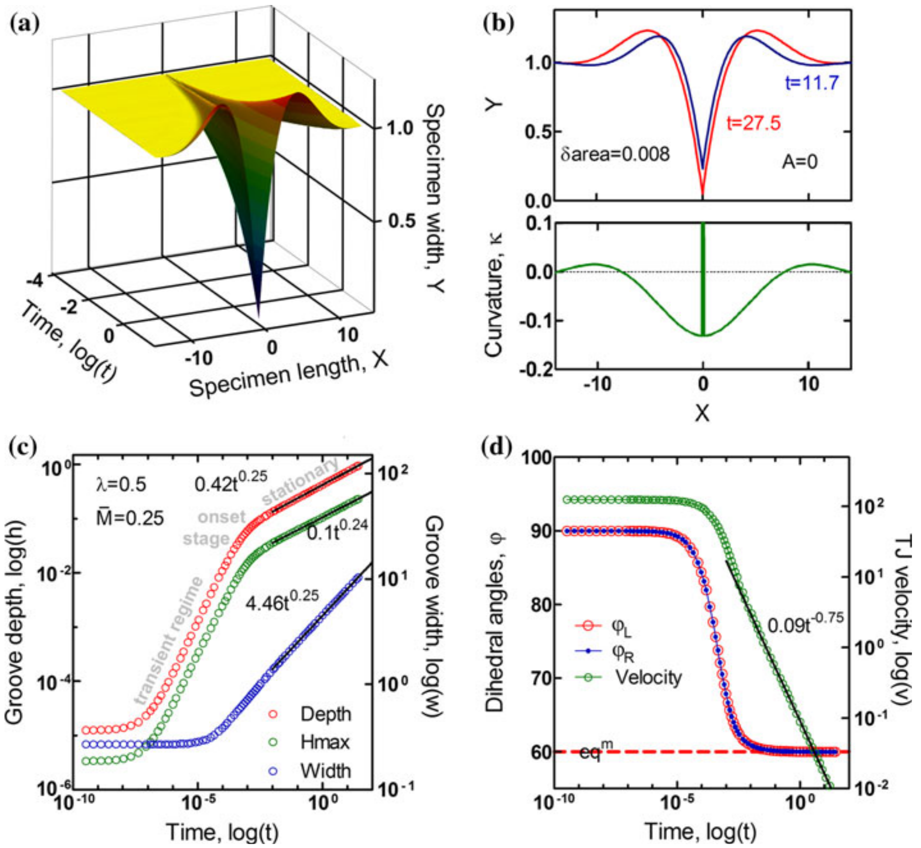

**Fig. 1** Isotropic thermal grooving for $\lambda = 0.5$, $\bar{M}^{\text{long}} = \bar{M}^{\text{trans}} = \bar{M} = 0.25$,**a** and **b** shows the GB profile, **c** kinetic data for groove depth, maxima, and width, **d** TJ velocity and the dihedral angles. The linear correlation factors ($R^2$) for depth, width, maxima, and velocity up to 5 decimals are 1.0, 0.99999, 0.99996, and 0.99974, respectively. Final time for failure is equal to $t_f = 27.5$ in normalized scale

mobilities $\tilde{M} = 100 - 1,000$ at the steady state regions for the finite and infinite extend test modulus, respectively. Here, one should remark that the following connection exists [21] between their normalized mobility denoted by $\tilde{M}$ and the normalized mobility defined in this article, namely, $\tilde{M} = \bar{\Omega}^{-1}\bar{M}^{\text{long}}$, where $\bar{\Omega}^{-1} = 1,000$. The median sector of the groove depth trajectory, which follows up a straight line in the double logarithmic scale, may be called as a transition or onset-stage. This sector corresponds to the upper part of the transient regime and follows up exponential time dependence in addition to the quadratic relationship with the WP. This sector is completely ignored in many experimental studies due to the fact that it covers rather a short life-time. It is also overlooked in many theoretical studies due to the improper boundary conditions such as the utilization of the equilibrium dihedral angles at the groove root, which is solely based on the reversible thermodynamics considerations [23].

In the normalized and scaled time and space domain, the following analytical expressions are obtained for the GB–TJ velocity and the GB groove height at the stationary state, and the stationary state plus the transient regime, respectively. Here, the first order reaction kinetics appears to dominate in the transient sector completely. It is also found that the onset of the stationary state regime is about $\bar{t}_{\text{onset}} = 0.01$ in the normalized time scale:

$$\bar{H}_{gb}(\bar{t},\lambda) = [1 - 9.7\exp(-\xi(\bar{t}-\bar{t}_o))] \times \left[\frac{4\lambda}{5}\left(\bar{t}^{1/4} - 0.01^{1/4}\right)\{0.459\lambda^2 + 0.17\lambda + 0.028\}\right] \tag{9}$$

and

$$\bar{V}_{gb} = \frac{\lambda}{5}\bar{t}^{3/4} \tag{10}$$

Here, $\xi$ and $\bar{t}_o$ are found to be $2 \times 10^3$ and $10^{-7}$, respectively. These are system parameters similar to $\bar{t}_{\text{onset}}$, and their values solely depend on the GB–TJ mobilities, as will be observed later in this section. In these experiments, the GB–TJ mobilities are selected in the range of $\bar{M}_{\substack{\text{long}\\ \text{trans}}} \subset (1 - 0.25)$, which may be called Mullins' capillary driven regime for a good reason.

Mullins [2] presented an equation for the groove depth, which reaches the stationary regime as: $h = 0.78\ m(Bt)^{1/4}$; in this notation $h$ is the depth measured from the initial flat surface, $m$ is the slope of the tangent line passing through the groove root $m = \tan(\theta)$; here $\theta$ is the complementary dihedral angle ($\theta = \pi/2 - \varphi$) which approximates to the WP for small values (small slope approximation; $\theta = a\sin(g_g/2\ g_\sigma) \approx g_g/2\ g_\sigma$). The parameter $B$ is a collection of physicochemical and kinetic constants, and it is defined by $B = D_s g_\sigma \Omega_\sigma^2 \nu/kT$; here $\Omega_\sigma$ is the mean atomic volume, $\nu$ is the surface concentration of diffusing atoms, $k$ is the Boltzmann's constant and $T$ is the absolute temperature. Since, this parameter is embedded into the time scale $\tau_o$, to compare the equations obtained from the regression analysis of the results of present study with Mullins' it is enough to divide the cofactors with the *tangent* of the WP ($\lambda = 0.5$). The result is $h = 0.42t^{0.25} = 0.77\tan(\lambda)t^{0.25}$; which is close to the equation given by Mullins. Mullins denotes the groove width with $s$ (separation between the two maxima) and gives its equation as: $s = 4.6(Bt)^{0.25}$, this is close to $w = 4.46t^{0.25}$, which we have obtained. The time law for the two maxima in Fig. 1c is $h_{\max} = 0.18\tan(\lambda)t^{0.24}$ and for the TJ velocity in (Fig. 1d) is $V = 0.09t^{-0.75}$, which can simply be regarded as the time derivative of the groove depth. Mullins gives the equation for the depth of the groove measured from the maximum of the surface to the groove root as: $d = 0.973\ m(Bt)^{1/4}$. This equation corresponds to the sum of the cofactors of our equations $h$ and $h_{\max}$; $0.77 + 0.18 = 0.95$. The time independent ratio of the groove width and depth was given by Mullins as $s/d = 4.73/m$ compared to our $4.69/\tan(\lambda)$. The linear correlation factors ($R^2$) for depth, width, maxima and velocity up to 5 decimals are 1.00000, 0.99999, 0.99996, and 0.99974, respectively. These values demonstrate the extreme long range stability in our computer simulation experiments.

Mullins' theoretical coefficients rely on the small slope approximation, yet the results presented in Fig. 1 demonstrate clearly that the front tracking method employed in our simulations is converging to Mullins' analytical solution for this relatively large value of the WP ($\lambda = 0.5 \rightarrow m = 0.577$). The time exponents and cofactors obtained in this study are definitely realistic numbers for the finite slopes and finite but large GB TJ mobilities $\left(\bar{M}^{\text{long}} \geq 0.1\right)$. Below this range, the time exponent shows dependence on the TJ mobilities [21] and assumes an upper limit of 0.5 where the upper bound of the normalized mobility becomes $\bar{M}^{\text{long}} \leq 0.001$.

For most of the metals in vacuum or inert atmospheres [29] $\lambda$ is on the order of 0.125–0.25, which yield slopes less than 0.3 (see Table 1 [30–35]). Thus, Mullins' small slope solution yielded reasonable results. However, for some surface active environments such as liquid metals or active gases $\lambda$ can even be close to unity [36]. Numerical solutions of the nonlinear fourth order differential equation describing the phenomena for finite slopes are also obtained by Robertson [36], and Zhang and Schneibel [37]. Both authors stated that as $m$ grows larger, the depth of the groove profile ($d = \alpha t^{1/4}$) becomes lower than the values assumed by Mullins' solution. Relevant figures from those authors are digitized and given in Fig. 2a together with the values obtained from the present study. In Fig. 2b, Robertson's [36] Fig. 6 is redrawn to show the deviation from the small slope approximation. In citing Robertson's work, Zhang and Schneibel [37] stated that Robertson's groove depth results are smaller than theirs and hence deviate further from Mullins' result for the linearized surface diffusion equation in the case of small dihedral angles, or large slopes. We may say the very same thing for Zhang and Schneibel's work [37] compared to ours by looking at Fig. 2a for small slopes. Nevertheless, both studies are in good agreement in general. In Fig. 2, the WP used in the experiment given in Fig. 1 ($\lambda = 0.5$) and the corresponding slope is shown by markers (dashed line) to indicate the level of agreement.

**Table 1** Selected values of grain boundary energy $g_g$ and crystal vapor surface energy $g_\sigma$ for various materials in ergs/cm$^2$, and corresponding WPs $\lambda$ and slopes $m$

| Material | $g_g$ | $g_\sigma$ | $\lambda = g_g/2g_\sigma$ | $M$ |
|---|---|---|---|---|
| Ag | 790[a] | 1,140[a] | 0.346 | 0.349 |
| | 375[b] | 1,100[b] | 0.191 | 0.195 |
| | 375[c] | 1,136[c] | 0.165 | 0.167 |
| Al | 625[a] | 1,140[d] | – | – |
| | 324[b] | 980[b] | 0.165 | 0.167 |
| Au | 364[a] | 1,485[a] | 0.123 | 0.124 |
| | 378[b,c] | 1,400[b,c] | 0.135 | 0.136 |
| Cu | 646[a] | 1,725[a] | 0.187 | 0.190 |
| | | 1,670[a] | – | 0.160[e] |
| | 625[b] | 1,780[b] | 0.176 | 0.178 |
| | 625[c] | 1,736[c] | 0.18 | 0.183 |
| | 654[f] | 1,725[f] | 0.187 | 0.190 |
| Fe | 780[a] | 1,950[a] | 0.200 | 0.204 |
| Ni | 690[a] | 1,725[a] | 0.200 | 0.204 |
| | 565 | 2,280[g,h] | 0.124 | 0.125 [g] |
| W | | 2,900[a] | – | – |
| | 1,400 | 2,800[h,i] | 0.25 | 0.26[i] |
| | 1,080[c] | 2,634[c] | 0.205 | 0.209 |

[a] Ref. [30], [b] Ref. [13], [c] Ref. [4], [d] Ref. [31], [e] Ref. [2], [f] Ref. [32], [g] Ref. [33], [h] Ref. [34], [i] Ref. [35]

Figure 3 shows the system response at different values of the WP. Following Robertson [36], to enable comparison with Mullins [2], groove profiles are normalized with

**Fig. 2** **a** The relation between depth cofactor ($d/t^{1/4}$) and the slope; **b** finite slope ($\tan(a\sin(\lambda))=\lambda/\sqrt{(1-\lambda^2)}$) (*upper curve*) and the small slope approximation ($\tan(\lambda)$) (*lower curve*) as a function of the WP

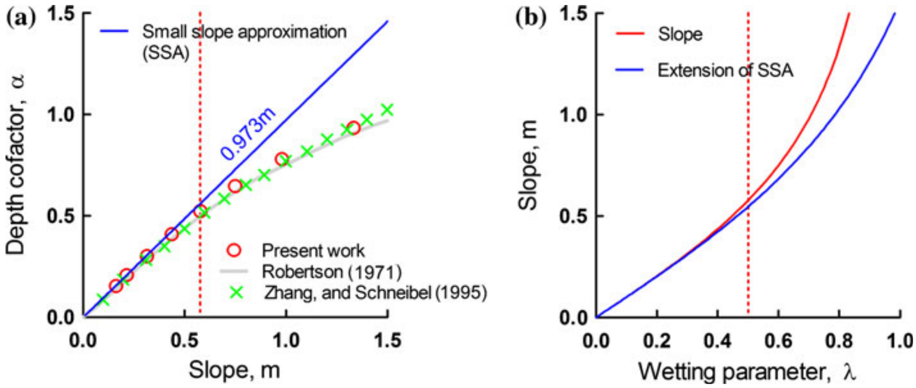

respect to $mt^{0.25}$ in $y$-axis and $t^{0.25}$ in $x$-axis in Fig. 3a. On this plot, each curve has a unit slope at $x/t^{0.25} = 0$, and it compares steady groove shapes for each $\lambda$, whose dimensions grow in proportion with $t^{0.25}$. In Fig. 3b, normalization is done with respect to unit depth and unit half width ($W$), where $y_0$ is the value of $y$ at $x = 0$. The curves labeled as $m \to 0$ are the curves calculated by Mullins [2] using small slope approximation. These two figures show that $h_{\max}$ decreases with increasing $\lambda$ (or $m$), for the stationary grooves; and the profiles become relatively steeper at the groove root and bends away more sharply with increasing $\lambda$ [36].

In Fig. 3c, we see that the transition time to stationary region (final linear region in the log–log plot) is approximately the same for all experiments. Lowering the WP prolongs the observation time of steady grooves hence the equilibrium dihedral angle is established at lower groove depths. The $0.973\tan(\lambda)t^{0.25}$ lines shown in the figure reflect the fact that changing $\lambda$ does not affect the time exponent, which is a function of mass transport mechanism. Experimentally calculated connections may be extracted from Fig. 2a by using $d = \alpha t^{1/4}$. The equilibrium dihedral angles in Fig. 3d can simply be calculated by taking arccosine of $\lambda$ according to the selected convention.

Ogurtani and Akyildiz [23] showed the existence of a transient regime and incorporated this regime into their penetration depth formula by stating that the rate of this evolution process in the transient regime obeys the first order reaction kinetics, and may be described by the exponential time dependence. This regime is totally

**Fig. 3** Thermal grooving for different WPs. Simulated profiles are normalized with respect to **a** $mt^{0.25}$ and $t^{0.25}$, **b** unit depth and unit half width. The $m \to 0$ curves are plotted using Mullins' profile function. Kinetic data for **c** the groove depth and **d** the dihedral angles

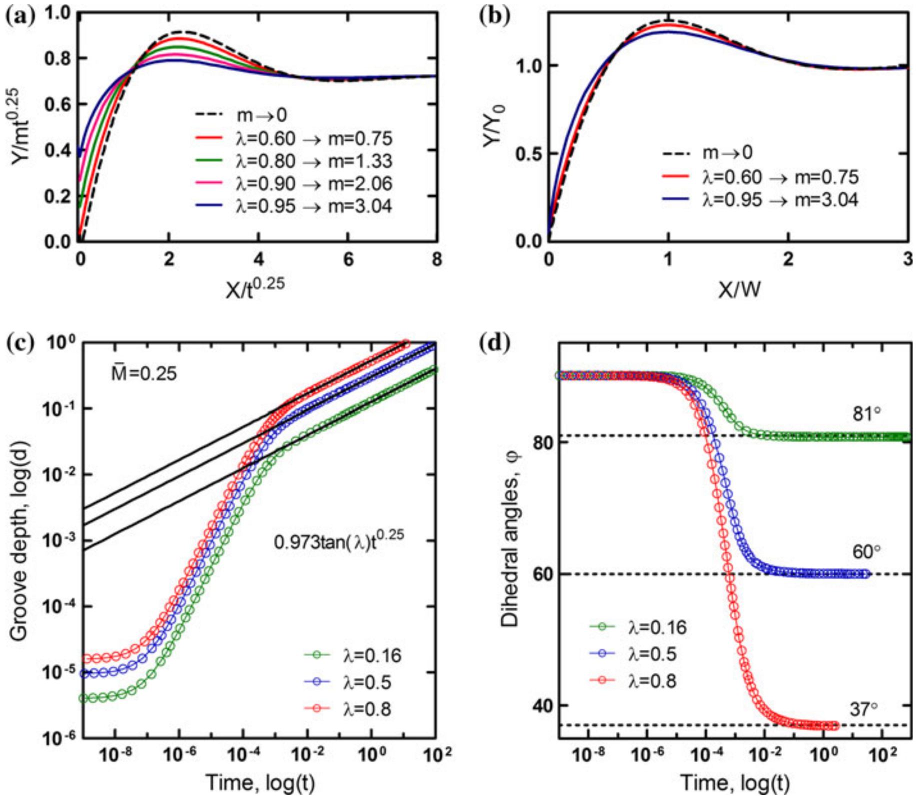

ignored by researchers employing Mullins' boundary condition at groove root (constant slope). On the other hand, Zhang et al. [26] in their grooving experiments with tungsten at 1,350 °C observed GB grooves with dihedral angles decreasing continuously. They found a time exponent of 0.44 for the depth of these grooves. They assumed that the change of the dihedral angle is stemming from a change in surface free energy during experimentation due to changes in the surface composition by segregation or adsorption. They explained the phenomena at this basis by noting that they were not aware of any article addressing changing dihedral angles in the model.

Zhang et al. [26] reported the values of average dihedral angles ($2\varphi$) for tungsten as $\{163.3^\circ, 157.4^\circ, 153.6^\circ, 150.1^\circ\}$ successively at 16, 32, 64, and 128 h. They have extracted this data from the 3D AFM images at each annealing time. This $\varphi$ data is plotted in Fig. 4a together with the results of the computer simulation experiment performed for $\lambda = 0.28$ and $\bar{M}^{\text{long}} = \bar{M}^{\text{trans}} = 0.25$. In the simulation experiment, $\varphi = 81^\circ$ is observed at $t = 10^{-4}$; this determines the scaling factor used in plot of Fig. 5a: $10^{-4}/16 = 2.5 \times 10^{-5}$.

It could be suggested from Fig. 4 that the changing dihedral angle phenomena reported by Zhang et al. [26] is due to the observation of nonsteady grooves. In this time interval, an attempt to determine a kinetic equation by regression analysis yields a time exponent of 0.46, which is very close to the reported value 0.44. Sachenko et al. [38] stated that the vapor pressure of tungsten at 1,350 °C is $2\times10^{-16}$ Pa and hence this evaporation condensation mechanism is not likely to operate. They also calculated the characteristic length above which the volume diffusion dominates surface diffusion in the order of 8 m, and after stating the groove widths measured in the experiments are in the order of 1 µm, they concluded that the dominant mass transport mechanism should be the surface diffusion. However, the time exponents observed by Zhang et al. [26] for the same experimental setup are physically meaningless at this basis and Fig. 4b clearly demonstrates the appearance of usual kinetic law for surface diffusion dominated mass transport on later times.

Figure 5 outlines the kinetic data for GB grooves having different longitudinal and transverse GB TJ mobilities, but for the same WP, $\lambda = 0.8$. It shows that the time spent at the transient regime could be increased by lowering the mobilities. Similarly for the low mobilities the equilibrium dihedral angle is hardly achieved. In order to be sure that the system is really in the stationary state regime; rather one has to wait for extremely long computation times [28].

The assumption of instantaneous formation of the equilibrium angle at the groove root highly depends on the TJ mobility. Since flux is proportional to mobility, an increase in mobility increases the evolution rate and hence decreases the time to observe stationary state grooves and vice versa.

Unlike the groove depth, no transient regime is observed for the groove width whose time evolution is given in Fig. 1c. Robertson [36] observes a slight decrease in the groove width cofactor with increasing slope, which does not depart more than 5% from the value of 4.6 as $m \rightarrow 0$. We did not observe a change greater than this amount. However, precise calculation of the width has a practical importance. Since its introduction in 1957, Mullins' theory is used extensively in determination of the surface diffusion coefficients ($D_s$). Once the active mass transport mechanism is confirmed (e.g. if surface diffusion, by

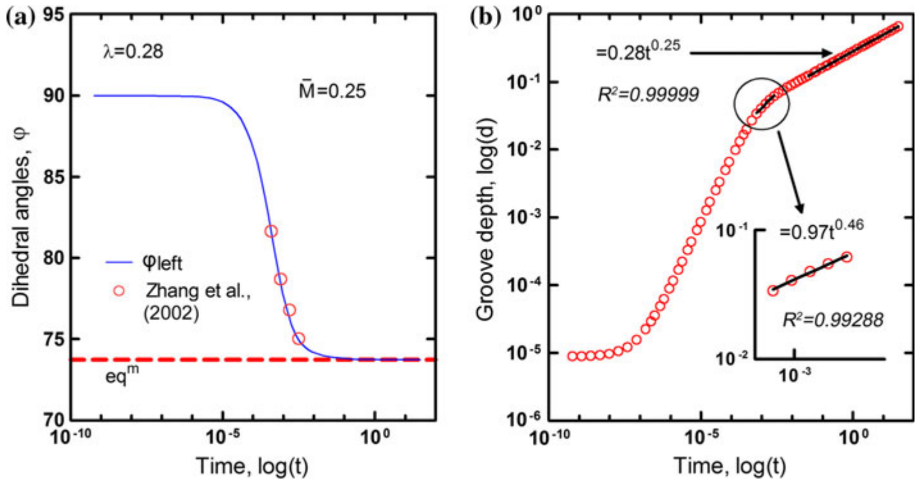

**Fig. 4** Thermal grooving for $\lambda = 0.28$ and $\bar{M}^{\text{long}} = \bar{M}^{\text{trans}} = \bar{M} = 0.25$. **a** kinetic data for the dihedral angles resulting from present simulation and reported by Zhang et al. [26], **b** kinetic data for the groove depth and the lines obtained from linear regression in the transient (knee-end) and stationary states; the first kinetic equation in the transient regime is $d = 0.97t^{0.46} = 3.38\tan(\lambda)t^{0.46} = 3.33\lambda/\sqrt{(1-\lambda^2)}t^{0.46}$ and the second one in the stationary regime is $d = 0.283t^{0.25} = 0.984\tan(\lambda)t^{0.25} = 0.97\lambda/\sqrt{(1-\lambda^2)}t^{0.25}$

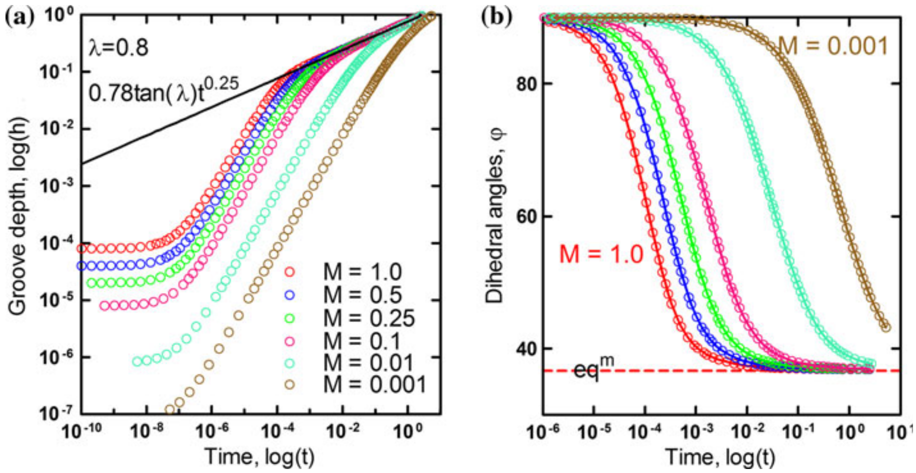

**Fig. 5** Thermal grooving by different TJ mobilities, $\bar{M}^{\mathrm{long}} = \bar{M}^{\mathrm{trans}} = \bar{M}$. Kinetic data for **a** the groove depth and **b** the dihedral angles

assuring groove grows in proportion with $t^{0.25}$), the ratio of the groove depth (or width) measurements taken at different times yield the $B$ parameter. Thereafter, provided that the surface energy is known, constant temperature experimentation gives the surface diffusivity. It is experimentally difficult to obtain reproducible measurements for the groove depth (scanning the vertical direction) either by interferometry (due to “tails” on the fringe pattern at the groove root [39]) or by scanning probe microscopy (SPMs) techniques (due to non zero tip diameter; see e.g. Sachenko et al. [38] for a detailed discussion). Because of these inconveniences most of the $D_s$ calculations involve measurements of groove width. Then, a value of 5% uncertainty may lead to $D_s$ within an accuracy of about 20% [36].

## Thermal grooving with anisotropic surface diffusivity

The angular part of anisotropic diffusion as introduced in the governing equation (Eq. 1) may be represented by $D(\theta, \phi; n) = 1 + A\cos^2\left[\frac{n}{2}(\theta - \phi)\right]$. Here, $\theta$ is the angle between the tangent vector of the contour line (diffusion path) of the sidewalls on the top surface and the global $x$-axis, which lies along the longitudinal axis of the bicrystal line having a length designated by $L$. $A$ is the anisotropy constant, which may be a few orders of magnitude. Where, $n$ corresponds to the $2\pi/n$ degrees of rotational symmetry (folding) associated with the zone axis of a given family of planes over which diffusion takes place. Similarly, the tilt angle $\phi$ is the angle between the major axis of the 2D diffusion map, along which diffusivity is maximum, and the global $x$-axis. The stability and instability regimes for the finite amplitude perturbations may be defined, respectively, by the following open intervals for the tilt angles: $(0 < \phi < \pi/n)$ and $(\pi/n < \phi < 2\pi/n)$, plus their periodic extensions.

In Fig. 6, several GB groove profiles obtained by computer simulations from symmetrically disposed bicrystals are presented for various fold numbers and tilt angles. A slight modification of the groove width and maxima is observed especially for the test samples having high fold numbers. These figures also indicate that the main departure from the isotropic case occurs when the tilt angle becomes $\phi = 3\pi/2n$. These modifications may be introduced into the Mullins’ solution by introducing two extra parameters (width and height adjustment factors) as it has been suggested by Ogurtani [40] to govern the anisotropy due to the surface free energy. It has also been observed that formation of secondary oscillations at the tails is also a strong function of anisotropy.

In Fig. 7, the normalized failure times due to film agglomeration are plotted as a function of the tilt angle for different fold numbers. The angular averaged normalized isotropic failure time, which may designated as the effective isotropic failure time, is given by $\langle t\rangle_{\mathrm{F}} \equiv \bar{t}_{\mathrm{F}}/(1 + A/2) \to \bar{t}/6$ where $\bar{t}_{\mathrm{F}} = 27.5$. This is also given in the same figure. The shortest lifetime is achieved in the case of isotropic surface diffusivity; and we also observed that the lifetime decreases as the degree of folding increases, which is in complete accord with isotropic case as a limiting behavior. This fast failure is because of the introduction of the more fast diffusion paths into the scenario. For 2-fold symmetry (which corresponds to $\{110\}$ planes in an fcc crystal), the longest lifetime is at ±90° orientation, for 4-fold it is at ±45°, and for 6-fold at ±30°. That means one has the following connection between the longest lifetime and the fold number: $\phi_{\max} = \pi/n$. The other orientations may be grouped as the fatal bicrystal textures, which may cause very short lifetimes.

In Fig. 8, several GB groove profiles obtained by computer simulations from a set of asymmetrically disposed bicrystals are presented for various fold numbers and tilt

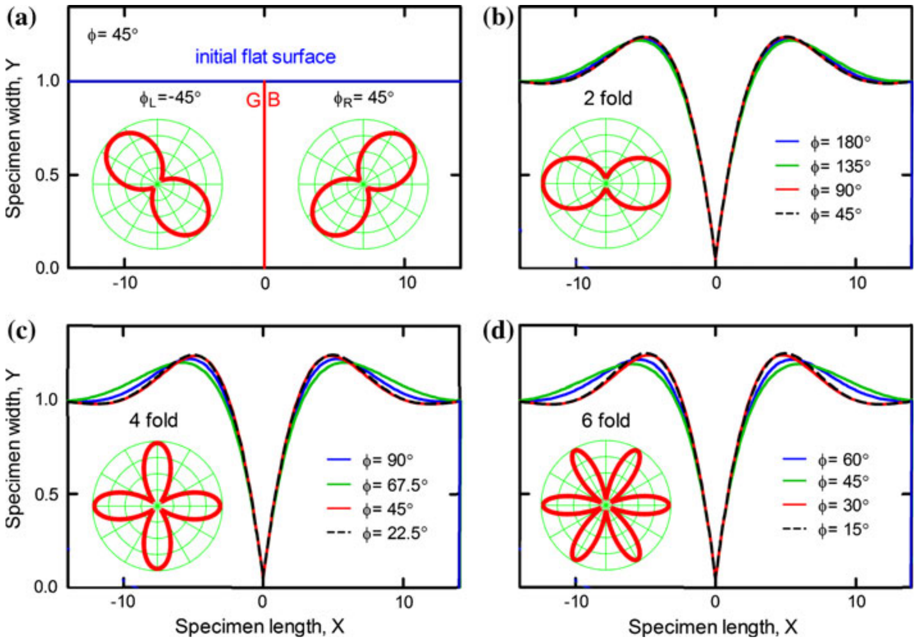

**Fig. 6** The symmetrically disposed grain boundary thermal grooving with anisotropic surface diffusivities with $A = 10$. **a** Schematic drawing showing initial flat surface and symmetric grain orientations for $n = 2$, $\phi = \pm 45^\circ$, **b** 2-fold symmetry with ±45, ±90, ± 135, and± 180° tilt angle, **c** 4-fold symmetry with ±22.5, ±45, ±67.5 and ±90° tilt angle, **d** 6-fold symmetry with ±15, ±30, ±45, and ± 60° tilt angle. Experiments are performed for the following physicochemical parameters: $\bar{M}^{\text{long}} = \bar{M}^{\text{trans}} = \bar{M} \subset (1 - 0.25)$ and $\lambda = 0.5$

angles. Large modifications in the groove width and maxima are observed in these cases especially for low fold numbers. These figures also indicate that the main departure from the isotropic case occurs when the tilt angle becomes $\phi = \pi/n$. It has been also observed that formation of secondary oscillations at the tails is also a strong function of anisotropy.

In Fig. 9, the normalized failure times due to film agglomeration are marked as a function of the tilt angle for different fold numbers in the case of asymmetric bicrystal films. Here, the left hand grain orientation is kept constant for a given tilt angle as described in the insert, whereas the right side grain orientation is altered in a stepwise manner.

This set of experiments has shown that the longest lifetime is achieved when the left hand grain orientation is set at $\phi_L = \pi/n$, regardless of the fold number. For the two, four and 6-fold symmetries the longest lifetime is at +90°, +45°, and +30° tilt orientations when the left hand grain oriented along the zero and $\phi_L = \pi/2n$ directions. Here, the positive sign indicates anti-clock wise rotation or tilting of the major diffusivity axis. It seems that in general the 6-fold symmetry, which corresponds to the {111} set of top surface planes in fcc structure, has the most favorable texture as far as the prolonged lifetime is concerned.

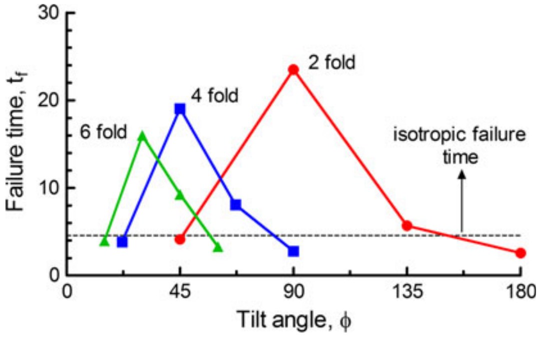

**Fig. 7** Failure times due to film agglomeration for different tilt angles and fold symmetries

## Conclusions

We performed extensive computer simulations on the surface diffusion induced and capillary driven GB thermal grooving with finite slopes (i.e. no small slope assumption). The simulations produced time independent groove profiles having linear dimensions growing with $t^{1/4}$ for large TJ mobilities in the range of $\bar{M}^{\text{long}} \geq 0.1$. These results are in good agreement with the analytic (small slope) solution obtained by Mullins [2] for large TJ mobilities. However, the situation is completely different for the low and medium mobility ranges $\bar{M}^{\text{long}} \leq 0.001$: the time exponent is observed to approach gradually to $\Rightarrow 0.5$ at the stationary state regime. These stationary nonequilibrium states (according to the definition of Prigogine [41]) are attained after the transient regimes, which obey the first order reaction kinetics [23].

The transient regime in general appears to be important in interpreting experimental results, especially with low TJ mobilities, where the stationary state is hardly achieved. This is demonstrated by introducing an analysis of experimental thermal grooving data reported for tungsten in the literature [26], which strictly correlates the observed “changing dihedral angle” phenomena to the transient grooving behavior.

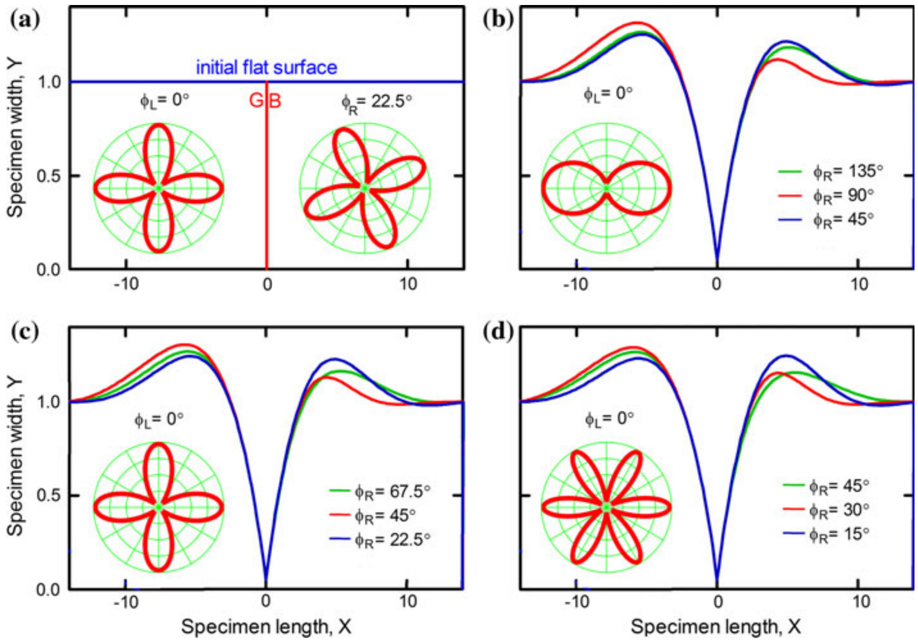

**Fig. 8** Thermal grooving for the asymmetric bicrystals with anisotropic surface diffusivities with $A = 10$ and left hand side grain's tilt angle, $\phi_{\mathrm{L}} = 0^\circ$ for: **a** schematic drawing showing initial flat surface and grain orientations for $m = 2$, $\phi_{\mathrm{R}} = +22.5^\circ$ **b** 2-fold symmetry with $\phi_{\mathrm{R}} = +45, +90$, and $+135^\circ$, **c** 4-fold symmetry with $\phi_{\mathrm{R}} = +22.5$, $+45$, and $+67.5^\circ$, **d** 6-fold symmetry with $\phi_{\mathrm{R}} = +15, +30$, and $+45^\circ$. Experiments were performed for the following physicochemical parameters: $\bar{M}^{\mathrm{long}} = \bar{M}^{\mathrm{trans}} = \bar{M} \subset (1 - 0.25), \lambda = 0.5$

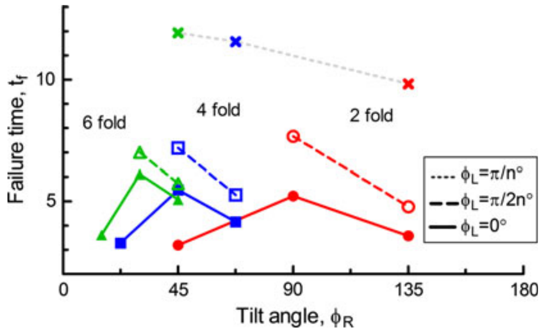

**Fig. 9** Failure times due to film agglomeration for different textures with $A = 10$. *Right*, *middle*, and *left* series represent 2-, 4-, and 6-fold symmetries, respectively. *Solid lines* represent the failure time data at $\phi_{\mathrm{L}} = 0^\circ$, *dashed* and *dotted* lines represent corresponding data at $\phi_{\mathrm{L}} = \pi/2n^\circ$, and $\phi_{\mathrm{L}} = \pi/n^\circ$, respectively, where '$n$' is the fold number. Experiments were performed for the following physicochemical parameters: $\bar{M}^{\mathrm{long}} = \bar{M}^{\mathrm{trans}} = \bar{M} \subset (1 - 0.25)$, $\lambda = 0.5$

As far as the anisotropic surface diffusivity is considered, we found that the groove penetration rate increases for the symmetrically disposed bicrystals as the degree of folding increases, even though the overall morphology is not affected critically. The situation is more severe for the asymmetric bicrystals, where one observes almost a factor of three reduction in the lifetime compared to the symmetric case. However, the 6-fold symmetry becomes now the more favorable texture instead of 2-fold for the top surfaces of asymmetric bicrystals as far as the prolonged lifetime for the film agglomeration is concerned (see Figs. 7, 9). It has also been observed that formation of secondary tail oscillations in the groove profile is more pronounced, and a strong function of anisotropy.

**Acknowledgements** Thanks are due Dr. Aytac Celik of METU for his valuable comments on the article. We also thank the anonymous reviewer, who pointed out the critical role played by the angular averaging procedure in obtaining the effective isotropic failure time for comparison. This work was partially supported by the Turkish Scientific and Technological Research Council, TUBITAK through a research Grant No.107M011.

## References

1. Tritscher P, Broadbridge P (1995) Proc R Soc Lond A 450:569
2. Mullins WW (1957) J Appl Phys 28:333
3. Gibbs W (1948) Thermodynamics, vol I. Yale University Press, New Haven
4. Murr LE (1975) Interfacial phenomena in metals and alloys. Addison-Wesley, Massachusetts
5. Young T (1805) Philos Trans R Soc Lond 95:65
6. Rabkin E, Klinger L, Semenov V (2000) Acta Mater 48:1533
7. Klinger L, Rabkin E (2001) Interface Sci 9:55
8. Xin T, Wong H (2003) Acta Mater 51:2305
9. Zhang W, Sachenko PP, Gladwell I (2004) Acta Mater 52:107
10. Klinger LM, Chu X, Mullins WW, Bauer CL (1996) J Appl Phys 80:6670
11. Nathan M, Glickman EE, Khenner M, Averbuch A, Israeli M (2000) Appl Phys Lett 77:3355

12. Khenner M, Averbuch A, Israeli M, Nathan M, Glickman EE (2001) Comput Mater Sci 20:235
13. Liu CY, Lee S, Chuang TJ (2001) Mater Sci Eng B Solid 86:101
14. Wang WL, Lee S, Chuang TJ (2002) Philos Mag A 82:955
15. Chuang TJ, Rice JR (1973) Acta Metall 21:1625
16. Pharr G, Nix WD (1979) Acta Metall 27:1615
17. Martinez L, Nix WD (1982) Metall Trans A 13:427
18. Igic P, Mawby PA (1999) Solid State Electron 43:255
19. Ogurtani TO (2006) J Chem Phys 124:144706
20. Ogurtani TO, Oren EE (2005) Int J Solids Struct 42:3918
21. Ogurtani TO (2006) Phys Rev B 73:235408
22. Oren EE, Ogurtani TO (2002) In: Ozkan CS, Cammaratai RC, Freund LB, Gao H (eds) Thin films: stresses and mechanical properties IX, MRS symposia proceedings No. 695. Materials Research Society, Pittsburgh
23. Ogurtani TO, Akyildiz O (2005) J Appl Phys 97:093520
24. Ogurtani TO, Akyildiz O, Oren EE (2008) J Appl Phys 104(1):013518
25. Ogurtani TO, Akyildiz O (2008) Int J Solids Struct 45:921
26. Zhang W, Sachenko PP, Schneibel JH (2002) J Mater Res 17:1495
27. Yeremin EN (1979) The foundations of chemical kinetics. MIR Publishers, Moscow
28. Ramasubramaniam A, Shenoy VB (2005) Acta Mater 53:2943
29. Shewmon PG (1966) In: Margolin H (ed) Recrystallization, grain growth and textures. American Society for Metals, Metals Park, Ohio
30. Hirth JP, Lothe J (1968) Theory of dislocations. McGraw-Hill, New York
31. Smith U, Kristensen N, Ericson F, Schweitz J (1991) J Vac Sci Technol A 9:2527
32. Chen N, Li Z, Wang H, Sun J (2007) J Appl Phys 101:033535
33. Ogurtani TO (2009) J Cryst Growth 311:1584
34. Gao H (1991) Int J Solids Struct 28:703
35. Binh V, Chaudier M, Couturier J, Uzan R, Drechsler M (1976) Surf Sci 57:184
36. Robertson WM (1971) J Appl Phys 42:463
37. Zhang W, Schneibel JH (1995) Comput Mater Sci 3:347
38. Sachenko PP, Schneibel JH, Swadener JG, Zhang W (2000) Philos Mag Lett 80:627
39. Gjostein NA (1963) In: Robertson WD, Gjostein NA (eds) Metal surfaces: structure, energetics and kinetics. American Society for Metals, Metals Park, Ohio
40. Ogurtani TO (2007) J Appl Phys 102:063517
41. Prigogine I (1961) Thermodynamics of irreversible processes. Interscience Publisher, New York